Co$_3$O$_4$ nanofibers compounded with Pt/C as efficient bifunctional electrocatalysts for rechargeable Zn-air battery

Weimin Yang[1,*] (iD), Xiaoyu Wang[2], Yufei Yan[2], and Xifeng Ding[2,*]

[1] *Physics Labotory, Industrial Training Center, Shenzhen Polytechnic, ShenZhen 518055, China*
[2] *School of Materials Science and Engineering, Nanjing University of Science and Technology, Nanjing 210094, China*

ABSTRACT

Exploring efficient bifunctional electrocatalysts is critical for metal-air battery commercialization. Co$_3$O$_4$ produced by electrospinning was combined with Pt/C via ultrasonic vibration in this study. As a bifunctional oxygen evolution reaction (OER) and oxygen reduction reaction (ORR) electrocatalyst, Co$_3$O$_4$@Pt/C nanofibers were employed. The Co$_3$O$_4$@Pt/C nanofibers with a mass ratio of 1:1 (CP11) show excellent OER activity. It outperforms commercial Pt/C and Co$_3$O$_4$ electrocatalysts with a low overpotential (442 mV) and Tafel slope (71.36 mV dec^{-1}) at 10 mA cm^{-2}. With a half-wave potential of 0.74 V and diffusion limiting current density of 4.3 mA cm^{-2}, CP11 provides exceptional catalytic activity for ORR. The expanded surface area of Co$_3$O$_4$ nanofibers and the unique interaction between the Pt/C and metal oxides may be responsible for the high bifunctional catalytic activity of Co$_3$O$_4$@Pt/C nanofibers. More importantly, the zinc-air battery based on CP11 has a 0.64 V charging-discharging voltage gap and long-term stability. The improved OER/ORR bifunctional performance of Co$_3$O$_4$@Pt/C demonstrates the feasibility of using it in high-power energy storage and conversion devices.

1 Introduction

The public's interest in metal-air batteries as efficient energy storage and conversion devices is growing exponentially. Zinc-air batteries, for example, offer a high theoretical energy density (1084 Wh kg[-1 [1, 2]]), are environmentally friendly, and are inexpensive. However, the stagnant kinetics of oxygen evolution reaction (OER) and oxygen reduction reaction (ORR) caused by the multistep proton-electron transfer, limits the application of secondary Zn-air batteries [3, 4], which requires a large overpotential to reach the desired current density [5, 6]. As a result, highly effective electrocatalysts with quick OER/ORR kinetics are required [7, 8].

Pt/C [9, 10] is the most well-known ORR catalyst, while precious metal oxides like IrO$_2$ and RuO$_2$ are

Address correspondence to E-mail: ywm13@163.com; dingxifeng@njust.edu.cn

Springer

known for their high OER activity [6, 11]. However, their rarity and high cost limit their practical applications. Furthermore, most precious metal oxides are incapable of achieving bifunctional OER and ORR catalytic activity at the same time. Therefore, non-precious metal oxides, such as perovskite [12–14] and spinel oxides [15–17] have drawn great attention. Among them, cobalt-based oxides are considered superior catalysts due to their high catalytic performance [15, 17–23]. However, their poor conductivity and inferior ORR catalytic activity make them unsuitable as bifunctional catalysts for metal-air batteries. As a result, a lot of effort has gone into improving their bifunctional catalytic activity. Xu et al. [24] designed an efficient Co_3O_4 electrocatalyst by plasma engraving. The superior OER catalytic activity was attributed to generated oxygen vacancies, enlarged surface area, and more Co^{2+}. Chemical treatment is an effective technique for improving OER catalytic activity [25], however, chemically treated electrocatalysts are not suitable for zinc-air batteries due to their low ORR performance. Compounding metal oxide with carbon material is one of the effective methods to improve the bifunctional catalytic activity of non-precious metal oxides. Ma et al. [15] used $NaBH_4$ reduction to produce a reduced $CoFe_2O_4$/graphene (r-CFO/rGO) with a high surface area and abundant oxygen vacancies, as well as a superior OER activity with a smaller Tafel slope (68 mV dec^{-1}), lower overpotential (300 mV), and better long-term stability. Wang et al. [26] designed core-shell-structured $Co@Co_4N$ nanoparticles ($Co@Co_4N$/MnO-NC), which showed superior OER/ORR activity owing to enhanced conductivity and higher O_2 transport from a porous carbon frame. Elumeeva et al. [27] used composite metal oxides with high-purity oxidized-multi-walled carbon nanotubes (MWCNTs). They found these composite electrocatalysts have high catalytic activity for OER/ORR and superior long-term stability. Han et al. [16] developed $NiCo_2S_4$ nanocrystals composite with nitrogen-doped carbon nanotubes ($NiCo_2S_4$/N-CNT) and found these composite catalysts exhibit low charge and discharge voltage (∼ 0.63 V), high efficiency, and stability. These composite catalysts have higher OER catalytic activity and enhanced ORR catalytic activity, but the ORR catalytic activity is still below that of the benchmark catalyst Pt/C. Cobalt-based catalysts exhibit high OER activity and long-term stability [24, 28], but their ORR activity is not

satisfactory. The ORR performance of metal oxide catalysts could be increased when Pt/C was used as the ORR catalyst [9, 10]. Thus, composite catalysts consisting of cobalt-based spinel metal oxides and Pt/C are expected to achieve the bifunctional effect on OER and ORR catalysis.

Increasing specific surface area is also an effective way to improve catalytic activity. Therefore, more and more researchers are trying to design oxides as nanostructures to enlarge the surface area [29, 30]. The electrocatalytic activities of spinel catalysts are unsuitable due to their low surface area. Ji et al. [31] synthesized $CoNC@MoS_2$/CNT films by electrospinning method. The porous structure of these films, together with their unique architecture, provides excellent stability and conductivity. The large specific surface area of the electrocatalysts provided more active sites for OER and ORR, which facilitated mass and electron transport during water splitting [1, 32–34].

In this work, we present an effective electrospinning method for fabricating Co_3O_4 nanofibers composited with 20wt% Pt/C. The electrocatalytic activities of the $Co_3O_4@Pt/C$ nanofibers for OER/ORR in alkaline media have been conducted by a three-electrode method. These nanofibers exhibited improved bifunctional electrocatalytic activities and long-term stability in alkaline solutions.

2 Experimental section

2.1 Synthesis and fabrication

A nanofibers spinel oxide Co_3O_4 was synthesized by a simple electrospinning technique. We dissolved 1.5 g PVP in 4.25 g absolute ethanol and 4.25 g N, N-dimethylformamide (DMF) and stir for 6 h to prepare the precursor solution. Then, added 1.2 mmol of cobalt nitrate into this solution and stir for 12 h. We loaded the solution in a syringe. To collect fibers, a strong electric field (16 kV) was applied. The solution will shoot at a rate of 1 mL h^{-1} with a target placed 14 cm away from the needle. The collected nanofibers were heated at a slow rate of 1 °C min^{-1} until 400 °C for 2 h.

20wt% Pt/C were weighed in the beaker according to a mass ratio of 1:1, 1:2, and 2:1 with Co_3O_4, respectively. Then, 50 mg of the obtained Co_3O_4 and weighed Pt/C (50 mg, 100 mg, and 25 mg for a mass

ratio of 1:1, 1:2, and 2:1) were dissolved in 30 mL absolute ethanol and ultrasonically vibrated for 2 h to make the two catalysts fully mixed. The mixed solution was dried at 80 °C. The Co_3O_4@Pt/C composite catalysts with a mass ratio of 1:1, 1:2, and 2:1 were denoted as CP11, CP12, and CP21, respectively.

2.2   Catalyst characterization

Model XRD-6100, an X-ray diffractometer was used to study the crystalline structure. The XRD tests were performed at 40 kV and 30 mA in two-theta range of 20–80° at a scan rate of 6° min⁻¹. The surface morphologies of samples were examined by field-emission scanning electron microscope (Model FE-SEM, Quant 250FEG) with a test voltage of 20 kV.

2.3   Electrochemical measurements

The electrocatalytic activity test was measured by a rotating disk electrode (Model ATA-1B) and an electrochemical workstation (Model CHI660E). The three-electrode system consists of a working electrode (glass carbon GC), reference electrode (Ag|AgCl filled with saturated KOH), and counter electrode (Pt). The working electrode was prepared by dissolving 6 mg catalyst in 0.5 mL deionized water, 0.5 mL isopropanol, and 20 μL 5wt% Nation. After ultrasonication, 4 μL of the catalyst ink was added onto a GC electrode (0.07 cm²) and then dried at room temperature. The loading of catalyst on glassy carbon is 0.33 mg cm⁻². The GC electrode was polished by α-Al₂O₃ (0.3 μm) slurry on a polishing cloth before each test. 0.1 M KOH saturated with oxygen was used as an electrolyte.

The working electrodes were activated by a cyclic voltammetry test in 0.5 ~ 1 M KOH in the scan range of −1.0 ~ 1.0 V. The linear sweeping voltammograms (LSVs) measurements were conducted at a sweep rate of 0.005 V s⁻¹ under oxygen saturation. Electrochemical impedance spectroscopy (EIS) tests were carried out in the frequency range of 0.1 Hz−100 kHz. The stability tests were conducted by accelerated linear sweeping voltammogram measurements with a sweep rate of 0.1 V s⁻¹.

2.4   Zn-air battery

The rechargeable zinc-air battery was assembled using a homemade air cathode. The catalyst ink was dropped onto carbon clothes and dried at room temperature was used as an air cathode. A polished zinc plate was used as the anode and 6 M KOH with 0.2 M ZnCl₂ was used as electrolyte. The battery performance was tested by the electrochemical workstation. The polarization curves were obtained with a scan voltage range of −1 to 3 V and a scan rate of 0.01 V s⁻¹. The LAND testing method was used to assess the stability of a homemade zinc-air battery, which was charged and discharged for 600 min. In addition, a Pt/C-based zinc-air battery was assembled and studied as a reference.

2.5   Calculation details

The equation of potentially converted to RHE:

$$Ag|AgCl + 0.947 = RHE \tag{1}$$

The overpotential is defined as the following formula [35]:

$$\eta = E(vs.RHE) - 1.23V \tag{2}$$

The number of electron transfers per O_2 participating in oxygen reduction reaction can be calculated by Koutecky-Levich equations:

$$\frac{1}{j} = \frac{1}{j_L} + \frac{1}{j_K} = \frac{1}{(B\omega^{1/2})} + \frac{1}{j_K} \tag{3}$$

$$B = 0.2nFC_0(D_0)^{2/3}v^{-1/6} \tag{4}$$

$$j_K = nFkC_0 \tag{5}$$

where j donates the current density; j_K represents the kinetic and j_L is diffusion-limiting current density; ω is the 1600 rpm electrode representing rotating speed; n is the number of transferred electrons; B represents the slope of the Kouthechy-Levich curve; F is 96,485 C mol⁻¹, representing the Faraday constant; v is the kinetic viscosity; C_0 is 1.2×10^{-3} mol L⁻¹ indicating the bulk concentration of O_2 and D_0 is about 1.9×10^{-5} cm² s⁻¹, indicating the O_2 diffusion coefficient in the solution of 0.1 M KOH.

3   Results and discussion

Spinel oxide Co_3O_4 nanofibers were fabricated via an electrospinning process (Fig. 1a). Figure 1b displays the X-diffraction (XRD) patterns of composite electrocatalysts, Pt/C and Co_3O_4. Most peaks of Co_3O_4
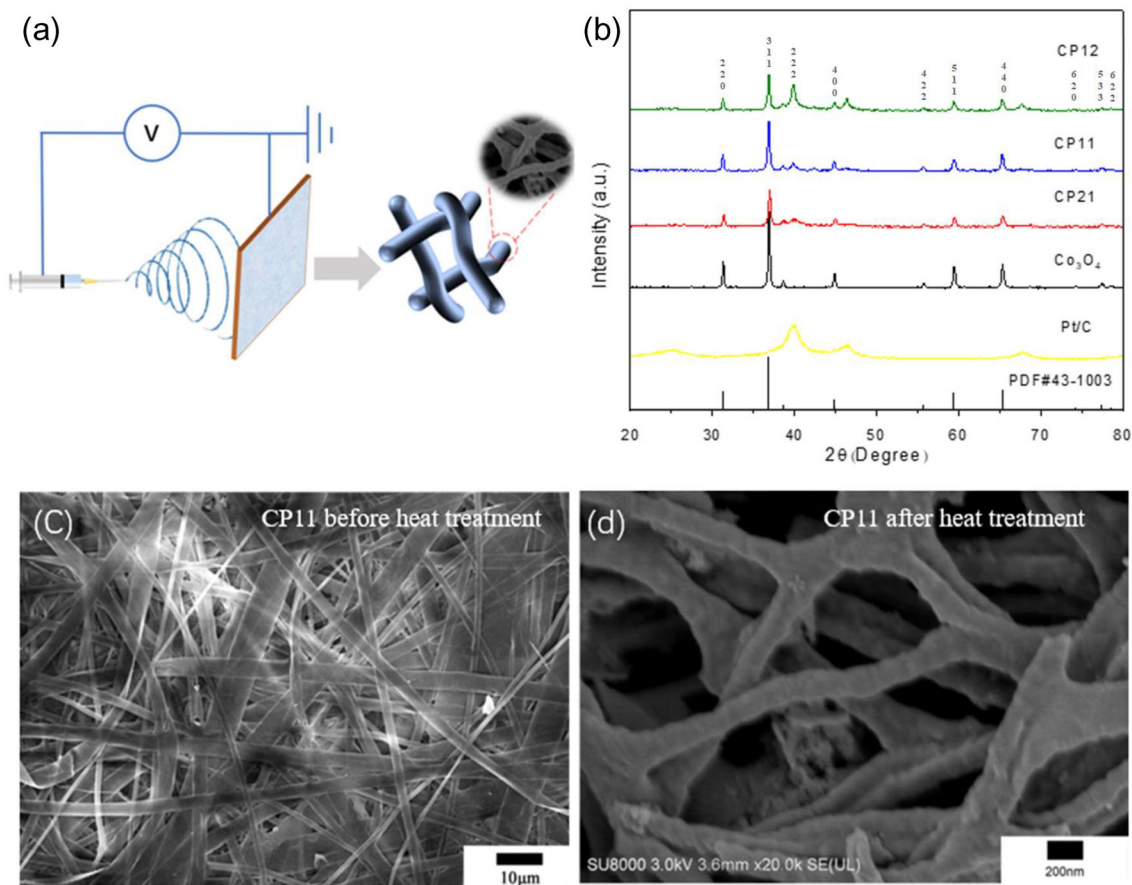
Fig. 1 **a** Schematic diagram of electrospinning; **b** XRD patterns of CP11, CP12, CP21, Co_3O_4, and Pt/C. SEM images of electrospinning samples **c** before 500 °C heat treatment; **d** after heat treatment

nanofibers are found to correspond to the spinel phase (JCPDS card # 43-1003). The XRD pattern of Pt/C in Fig. 1b was tested for the characterization of the composition of electrocatalysts. Both peaks around 40° and 46° correspond to the Pt and the broad peak around 23° is known as the peak of carbon [36]. The XRD patterns of composite electrocatalysts agree with Co_3O_4 and Pt/C and no other peaks of impurities were observed. It is noteworthy that with the increase of Pt/C content, the intensity of Pt increases, indicating that Pt/C has been successfully composited.

The scanning electron microscopy was applied to characterize the diameter and morphology of electrospinning Co_3O_4 nanofibers. The tubular structure and diameter of the fiber prepared by electrospinning can be related to the amount of solution PVP added [37]. Excessive conductivity of the solution causes instability of the jet in the spinning state, which leads to uneven diameter distribution of the fibers.

Electrospinning samples are also affected by the increased voltage and the distance between the target and needle tip. The parameters of the electrospinning are 15% by mass of PVP solution, 16 kV voltages, and 14 cm distance between the target and needle tip. Figure 1c–d shows the SEM images of the Co_3O_4 nanofibers synthesized in this condition. The as-spun precursory polymer fiber of Co_3O_4 with a diameter of $2 \sim 5$ μm can be firstly prepared (Fig. 1c). After heating for 2 h (400 °C, heating rate 2 °C/min), due to the pyrolysis of PVP, the diameter of these nanofibers is reduced ($200 \sim 500$ nm) and the surface of nanofibers (Fig. 1d) become very rough which means this sample may have more active sites. To synthesized composited catalysts, 20wt% Pt/C and Co_3O_4 were dissolved in 30 mL absolute ethanol and ultrasonically vibrated for 2 h to make the two catalysts fully mixed. Pt/C particles are attached to the surface of nanofibers to provide more ORR active sites. In order to provide more information about the

microstructure of catalysts, the N_2 adsorption/ desorption isotherms were conducted at −196 °C. The N_2 adsorption and desorption isotherm of all samples exhibited IV curve containing H3 hysteresis loop, implying that all composite catalysts possess mesoporous structure as shown in Fig. S1a–c. The specific surface areas were 20.1863 $m^2\,g^{-1}$, 31.7943 $m^2\,g^{-1}$, and 39.2876 $m^2\,g^{-1}$ for CP12, CP11, and CP21 (Fig. S1d).

Transmission electron microscopic (TEM) were conducted for further insight into the microscopic structure of CP11. It shows that the CP11 nanofibers comprise interconnected nanoparticles as shown in Fig. 2a. These interconnected nanoparticles would expose more active sites and improve mass diffusion during OER and ORR process. In addition, Pt/C attached to nanofiber surface which can improve the ORR performance of CP11. Furthermore, the EDS analysis of CP11 were conducted shown in Fig. 2b. It shows that Co, O, Pt, and C are evenly distributed, indicating that Pt/C has been successfully composited with Co_3O_4. The high-resolution transmission electron microscopy (HRTEM) image of CP11 were shown in Fig. 2c–e, in which the interplanar spacings of 0.246 and 0.287 nm correspond to (331) and (220) for Co_3O_4, respectively (Fig. 2d). And the interplanar spacings of 0.216 nm corresponds to (111) for Pt, suggesting that Pt/C are attached on the surface of Co_3O_4. Besides, ICP analysis indicating that the contents of Pt were consistent with the expected value, which is 0.35 wt%, 11.24 wt%, and 14.82 wt% for CP21, CP11, and CP12, respectively (Table S1).

Electrocatalytic activities of catalysts studied in this work were evaluated by a three-electrode configuration in 0.1 M KOH saturated with O_2. All the potentials were converted into the reversible hydrogen electrode (RHE) and were iR corrected. As a comparison, the benchmark catalysts Pt/C and IrO_2 were also investigated. To assess the electrochemical activities of Co_3O_4, the LSV, EIS, and ECSA were performed.

For OER, the electronic equation of the cobalt-based oxide catalyzed reaction is as follows [38]:
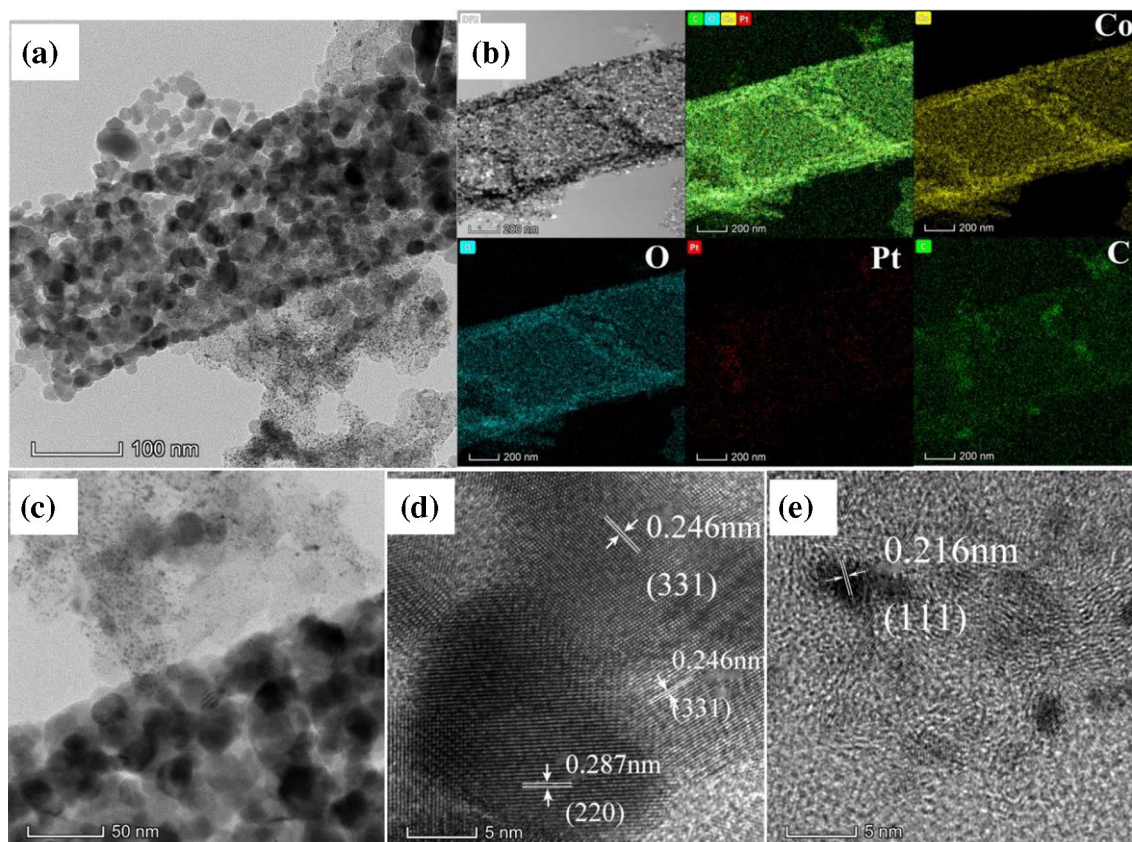

Fig. 2 a TEM images of CP11; **b** the corresponding energy-dispersive (EDS) elemental mapping of Co, O, Pt, and C; **c–d** the HRTEM images, corresponding FFT and inverse FFT pattern obtained masking the diffraction spot corresponding (331) and (220) lattice plane for Co3O4 (**d**) and (111) lattice plane for Pt **e**
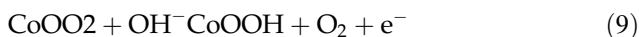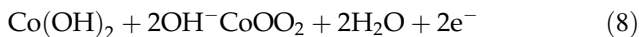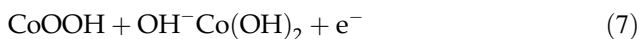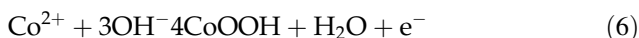
$$Co^{2+} + 3OH^- \, 4CoOOH + H_2O + e^- \tag{6}$$

$$CoOOH + OH^- \, Co(OH)_2 + e^- \tag{7}$$

$$Co(OH)_2 + 2OH^- \, CoOO_2 + 2H_2O + 2e^- \tag{8}$$

$$CoOO2 + OH^- \, CoOOH + O_2 + e^- \tag{9}$$

$$4OH^- \, O_2 + 2H_2O + 4e^- \tag{10}$$

Figure 3 shows the comparison result of OER activity between Co_3O_4@Pt/Cs, benchmark IrO_2 and Pt/C catalysts. LSV curves in Fig. 3a reveal the overpotential of composite catalysts at a current density of 10 mA cm^{-2} (452 mV, 442 mV, and 453 mV for CP21, CP11, and CP21, respectively) were smaller than the overpotential of Pt/C and Co_3O_4 (634 mV and 484 mV, respectively). Notably, the overpotential of the CP11was the smallest among all the samples and even smaller than that of IrO_2, indicating that CP11 nanofibers could be alternative to commercial IrO_2. In Fig. 3b, the OER Tafel slope of CP11 (71.36 mV dec^{-1}) was the lowest among all the samples

(75.81 mV dec^{-1} for CP12, 80.74 mV dec^{-1} for Co_3O_4, and 222.6 mV dec^{-1} for Pt/C). Interestingly, CP11 showed the highest activity for OER among the composite catalysts. Co_3O_4 as metal oxide shows poor conductivity, which is a shortcoming during the electrochemical reaction, but Pt and carbon materials are conductive. Thus, combining Co_3O_4 with Pt/C will greatly improve conductivity. Interestingly, the Tafel slopes of composite catalysts increase with the ratio of Pt/C, which means a decrease in catalytic activity. This is because more platinum-carbon catalytic active sites are inappropriate for OER.

In order to further understand the OER kinetics, the electrochemical impedance spectroscopy (EIS) measurements were carried out as well (Fig. 3). The fitting equivalent circuit given in the inset of Fig. 3 was used for the data analysis, in which R_s represents the solution resistance, R_1 is the resistance of charge transfer, R_2 stands for the resistance of mass transfer, and CPE_1, CPE_2 are the constant phase elements. As
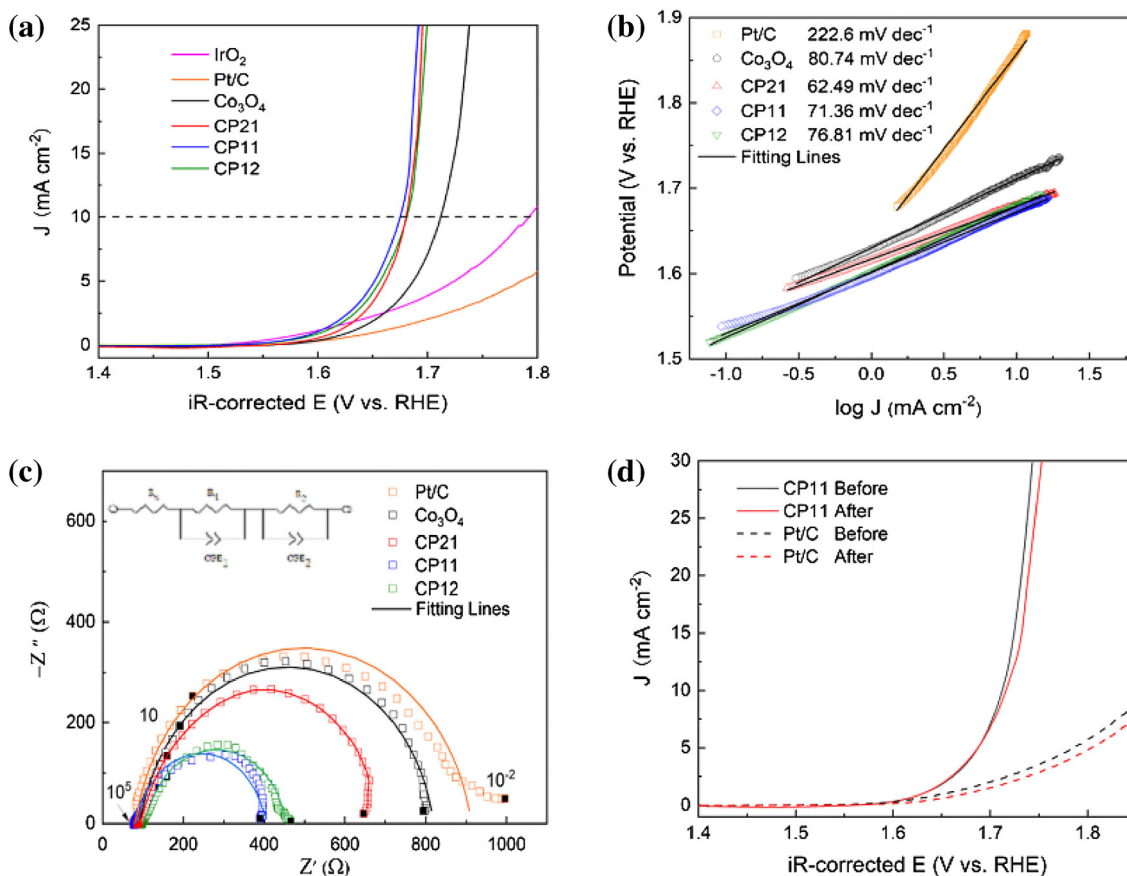

Fig. 3 a LSV curves recorded during oxygen evolution reaction for Pt/C, Co_3O_4, CP21, CP11, CP12, and IrO_2. **b** Tafel plots of Pt/C, Co_3O_4, CP21, CP11, and CP12. **c** Electrochemical impedance spectroscopy (EIS) of Pt/C, Co_3O_4, CP21, CP11, and CP12. The inset exhibits equivalent circuit model. **d** The initial LSV curves and LSVs after 1000 cycles of accelerated stability testing
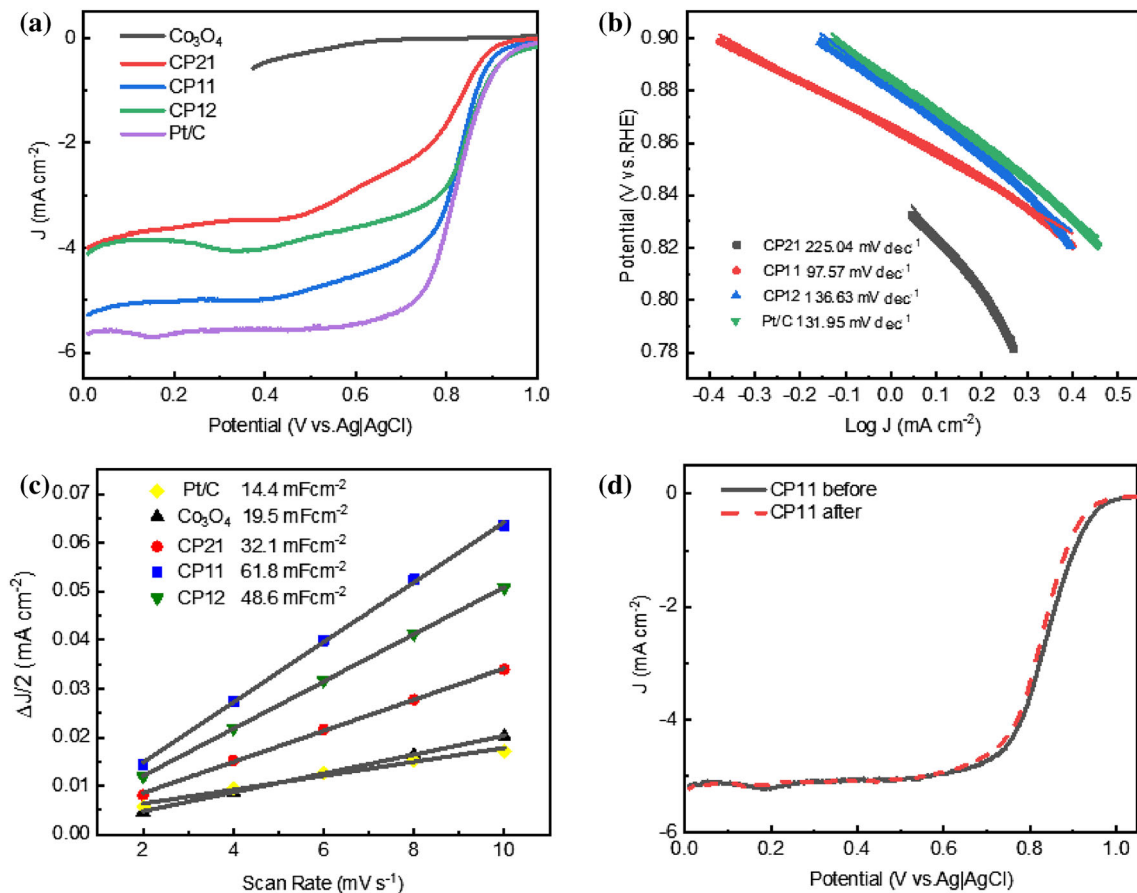
Fig. 4 **a** LSV curves recorded during oxygen evolution reaction for Pt/C, Co_3O_4, CP21, CP11, and CP12 at 1600 rpm; **b** Tafel plots; **c** the ECSA curves of catalysts; **d** The initial LSV curves and LSVs after 1000 cycles of accelerated stability testing

the Diameter of semicircle (related to R_1 and R_2) of CP11 was the smallest one among all composite samples (the measured impedances are in the order of CP11 < CP12 < CP21 < Co_3O_4 < Pt/C), it suggests that CP11 has a superior charge-transfer kinetics, which can lead to the splendid OER performance. The lower Tafel slopes together with the lower polarization resistance indicate the fastest OER kinetics of CP11 among the studied catalysts. This outcome is consistent with the LSV curve's conclusion. As shown in Fig. 3d, the LSV curve of CP11 nanofibers after 1000 cycles coincides with the curve before cycles, indicating its excellent stability.

Except for OER activity, the ORR activity is also crucial for an efficient catalyst. The limited current density of catalysts increases with rotating speed as shown in Fig. S2. Because of weak ORR activity, the performance of Co_3O_4 does not considerably improve with the spinning speed of the disc electrode during testing. The ORR catalytic performance of Co_3O_4@Pt/

C nanofibers is shown in Fig. 4. The half-wave potential ($E_{1/2}$) of the CP11 nanofibers was 0.820 V (~ 0.821 V for Pt/C, ~ 0.843 V for CP12, and ~ 0.786 V for CP21), and limiting current density (j_L) was found to be 5.02 mA cm^{-2}(~ 5.62 mA cm^{-2} for benchmark catalyst Pt/C, ~ 3.87 mA cm^{-2} for CP12, and 3.62 mA cm^{-2} for CP21). The half-wave potential and limiting current density of CP11 is close to those of commercial catalyst Pt/C, revealing the outstanding ORR performance of the CP11. The number of transferred electrons was around 4.2 for the CP11 according to the formula of the Kouthechy-Levich (K-L) plots, (Fig. S3), suggesting that the CP11 favors a nearly four-electron pathway. The Tafel slope of CP11 shown in Fig. 4b is 97.57 mV dec^{-1}, which is close to Pt/C (131.95 mV dec^{-1}) and lower than the slope of other composite catalysts in this study (136.63 mV dec^{-1} for CP12 and 225.04 mV dec^{-1} for CP21), reveals the fastest ORR kinetics of the CP11 among them. Different from OER, the Tafel slope of

Co_3O_4 (671.8 mV dec^{-1}) was much larger than other catalysts. In other words, more Co_3O_4 amount will result in inferior ORR catalytic activity. These values of CP11 correspond with the Pt/C, clearly demonstrate that the CP11 nanofibers can effectively promote the production of oxygen with a lower overpotential.

CV tests were used to determine the electrochemical surface area (ECSA) at various scan speeds (Fig. S4). As shown in Fig. 4c, the double-layer capacitance value (C_{dl}) corresponding to the slope of CP11 was 61.8 mF cm^{-2} which was higher than the value of CP12 (48.6 mF cm^{-2}), CP21 (32.1 mF cm^{-2}), Co_3O_4 (19.5 mF cm^{-2}), and Pt/C (14.4 mF cm^{-2}). The higher C_{dl} means a larger catalytic specific area [39], which has more activity sites and can promote electron transport. The ORR stability of CP11 was examined by LSV test as shown in Fig. 4d. The curves of CP11 do not show a significant decrease after cycles, indicating its superior stability.

The CP11 nanofibers show excellent catalytic activity (Table S2). Both the conductivity and larger surface area play an important role in bifunctional catalytic performance [40]. One of the main elements in improving the bifunctional activity of composite catalysts may be the synergistic effects of metal-oxygen and Pt/C. It has been reported that there are two possibilities to produce a synergistic effect in the composite material of Pt/C and metal oxide. One is that the oxide provides electrons to Pt to reduce its valence state, and then modifies the electronic structure on the surface of Pt, such as Pt-TaO$_x$ [9] and Pt-Fe$_3O_4$ [41]; the other is about the rate-determining step (RDS). In catalytic reactions, the process of

adsorption or desorption is often known as a reaction rate-determining step. For bifunctional composite catalysts consisting of Pt and metal oxides, when the ORR reaction occurs, Pt dominates the catalytic effect. The OH$^-$ produced from the surface of Pt will transport to the oxide surface and increase the number of ORR active sites to promote its catalytic effect [42]. In contrast, for OER, metal oxides play the catalytic role. The O_2 transport to Pt particles increases the number of OER activity sites to boost the catalytic effect [10]. Besides, the nanofiber structure with a larger specific surface area has more exposed active sites, which will lead to better electrochemical performance.

The improved electrocatalytic activity of CP11 inspired us to study its application in Zn-air batteries. Besides CP11, an air cathode fabricated with Pt/C was also tested for comparison purposes. The open circuit potential (OCP) the Zn–air battery using the CP11 catalyst was determined to be as high as 1.46 V (Fig. 5a). The specific capacity (normalized to the mass of consumed Zn) of CP11 was shown in Fig. 5b, the battery based on CP11 exhibited a high specific capacity (706 mAh g$_{Zn}^{-1}$) at a current density of 10 mA cm^{-2}. Fig. 6a depicts the polarization curves. In the discharge curve, the Pt catalyst exhibits a better catalytic effect. This is because, during discharge, an oxygen reduction reaction occurs, and the ORR catalytic effect of Pt/C is still better than that of the composite electrocatalyst CP11. Figure 6b presents the power density curves of Zn-air batteries based on CP11 and Pt/C. The power density of CP11-based battery (52.8 mWcm^{-2}) is similar to the density of catalyst Pt/C (57.82 mWcm^{-2}). In addition, we did charge-discharge cycling stability tests, as displayed
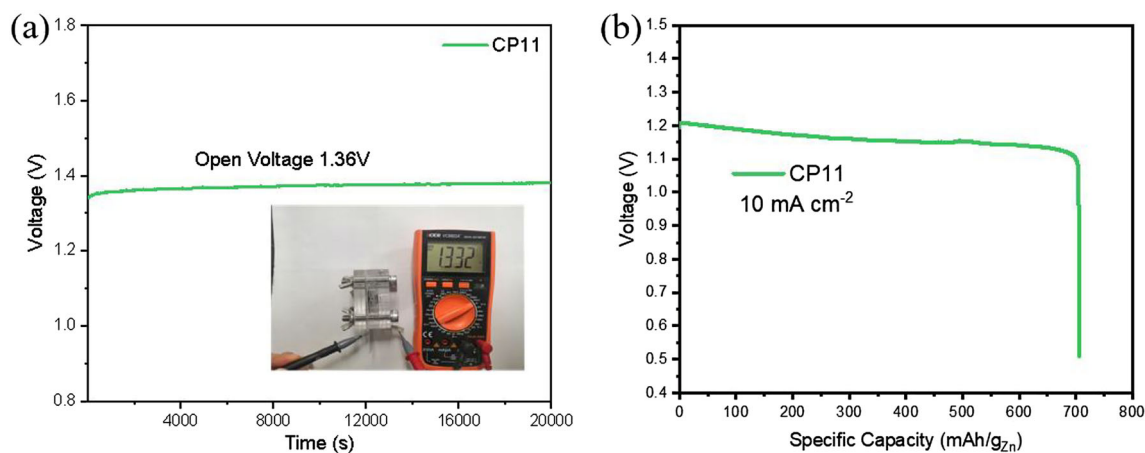

Fig. 5 a Open-circuit potential; **b** discharge curve of the Zn–air batteries based on CP11 catalyst at a current density of 10 mA cm^{-2}
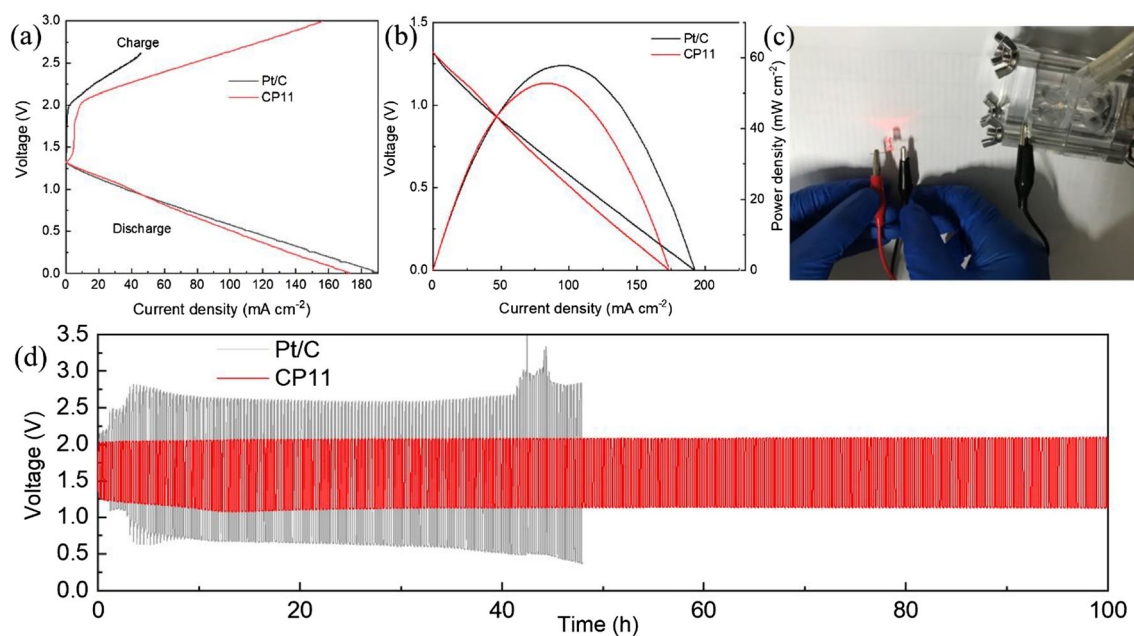
Fig. 6 a The polarization curves of discharge and charge; **b** Power density curves; **c** LED-lighted by Zinc-air battery based on CP11 and **d** discharge and charge curves with a constant current

in Fig. 6d. It was found that the battery based on CP11 maintained good stability during a 100-hours charge-discharge curve, but the Pt/C battery deteriorated dramatically after roughly 5 h. After the 100-hours charge-discharge test, the voltage gap of the battery based on the CP11 electrode increases from 0.65 to 0.84 V. However, the voltage gap of the Pt/C increase from 0.63 to 1.82 V during 50-hours charge-discharge test, which means that the stability of zinc-air battery based on the CP11 is better. The main factor limiting the use of noble metal catalysts in large areas is their poor stability. In other words, they can not maintain stability for an extended period. Therefore, synthesizing composite catalysts is an effective method to improve bifunctional catalysts' stability. Figure 6c demonstrates that the battery based on CP11 can successfully light a LED lamp (about 1.6 V).

4 Conclusion

To summarize, we have proposed a method for fabricating nanofibers spinel oxides Co_3O_4 using a Pt/C composite. The OER catalytic activity and stability of CP11 were both good. At $j = 10$ mAcm^{-2}, the overpotential was 442 mV, which is substantially lower than other catalysts in this study. The limited current density (4.3 mA cm^{-2}) and half-wave potential (74.1 mv dec^{-1}) of CP11 were both closed to Pt/C in the ORR test, demonstrating that compositing increased ORR activity. After 1000 accelerated cycle stability tests, it still demonstrated improved ORR catalytic activity. The CP11-based Zn-air battery has a power density of 53 mW cm^{-2} and can power an LED lamp. As a result, coupling a highly active OER catalyst with a highly active ORR catalyst Pt/C is a novel technique to make a bifunctional electrocatalyst. This will pave the way for the commercialization of zinc-air batteries.

Author contributions

WY: Data analysis, Writing—original draft, Writing—review & editing. XW: Visualization, Data collection. YY: Writing—review & editing. XD: Writing—review & editing, Methodology. All authors commented on previous versions of the manuscript. All authors read and approved the final manuscript.

Data availability

All data generated or analyzed during this study are included in this published article (and its supplementary information files).

Declarations

Conflict of interest The authors declare that they have no known competing financial interests or personal relationships that could have appeared to influence the work reported in this paper.

Supplementary Information: The online version contains supplementary material available at https://doi.org/10.1007/s10854-023-10287-z.

References

1. X. Chen, Z. Yan, M. Yu et al., Spinel oxide nanoparticles embedded in nitrogen-doped carbon nanofibers as a robust and self-standing bifunctional oxygen cathode for Zn–air batteries. J. Mater. Chem. A **7**, 24868–24876 (2019)

2. L. Liu, Y. Wang, F. Yan et al., Cobalt-encapsulated nitrogen-doped carbon nanotube arrays for flexible zinc-air batteries. Small Methods **4**, 1900571 (2020)

3. W. Bian, Z. Yang, P. Strasser et al., A $CoFe_2O_4$/graphene nanohybrid as an efficient bi-functional electrocatalyst for oxygen reduction and oxygen evolution. J. Power Sources **250**, 196–203 (2014)

4. C. Alegre, C. Busacca, A. Di Blasi et al., Electrocatalysis of oxygen on bifunctional nickel-cobaltite spinel. ChemElectroChem **7**, 124–130 (2020)

5. J.S. Lee, T.K. Sun, R. Cao et al., Metal–air batteries with high energy density: Li–air versus Zn–air. Adv. Energy Mater. **1**, 34–50 (2011)

6. H. Wang, J. Wang, Y. Pi et al., Double Perovskite $LaFe_xNi_{1-x}O_3$ nanorods enable efficient oxygen evolution electrocatalysis. Angew Chem. Int. Ed. Engl. **58**, 2316–2320 (2019)

7. Y. Li, M. Gong, Y. Liang et al., Advanced zinc-air batteries based on high-performance hybrid electrocatalysts. Nat. Commun. **4**, 1805 (2013)

8. M. Xu, D.G. Ivey, Z. Xie et al., Rechargeable Zn-air batteries: progress in electrolyte development and cell configuration advancement. J. Power Sources **283**, 358–371 (2015)

9. Z. Awaludin, J.G.S. Moo, T. Okajima et al., TaO_x-capped pt nanoparticles as active and durable electrocatalysts for oxygen reduction. J. Mater. Chem. A **1**, 14754 (2013)

10. N.R. Elezović, B.M. Babić, V.R. Radmilović et al., Pt/C doped by MoOx as the electrocatalyst for oxygen reduction and methanol oxidation. J. Power Sources **175**, 250–255 (2008)

11. Y.J. Sa, K. Kwon, J.Y. Cheon et al., Ordered mesoporous Co_3O_4 spinels as stable, bifunctional, noble metal-free oxygen electrocatalysts. J. Mater. Chem. A **1**, 9992–10001 (2013)

12. G. Li, S. Hou, L. Gui et al., Carbon quantum dots decorated $Ba_{0.5}Sr_{0.5}Co_{0.8}Fe_{0.2}O_3$- perovskite nanofibers for boosting oxygen evolution reaction. Appl. Catal. B (2019). https://doi.org/10.1016/j.apcatb.2019.117919

13. Y. Zhu, W. Zhou, Z.-G. Chen et al., $SrNb_{0.1}Co_{0.7}Fe_{0.2}O_{3-\delta}$Perovskite as a next-generation electrocatalyst for oxygen evolution in alkaline solution. Angew. Chem. Int. Ed. **54**, 3897–3901 (2015)

14. Y. Bu, G. Nam, S. Kim et al., A tailored bifunctional electrocatalyst: boosting oxygen reduction/evolution catalysis via electron transfer between N-doped graphene and perovskite oxides. Small **14**, e1802767 (2018)

15. Y. Ma, H. Zhang, J. Xia et al., Reduced $CoFe_2O_4$/graphene composite with rich oxygen vacancies as a high efficient electrocatalyst for oxygen evolution reaction. Int. J. Hydrog. Energy **45**, 11052–11061 (2020)

16. X. Han, X. Wu, C. Zhong et al., $NiCo_2 S_4$ nanocrystals anchored on nitrogen-doped carbon nanotubes as a highly efficient bifunctional electrocatalyst for rechargeable zinc-air batteries. Nano Energy **31**, 541–550 (2017)

17. W. Liu, J. Bao, L. Xu et al., $NiCo_2O_4$ ultrathin nanosheets with oxygen vacancies as bifunctional electrocatalysts for Zn-air battery. Appl. Surf. Sci **478**, 552–559 (2019)

18. M.A. Khalily, B. Patil, E. Yilmaz et al., Atomic layer deposition of Co_3O_4 nanocrystals on N-doped electrospun carbon nanofibers for oxygen reduction and oxygen evolution reactions. Nanoscale Adv. **1**, 1224–1231 (2019)

19. Z. Li, B. Li, J. Chen et al., Spinel $NiCo_2O_4$ 3-D nanoflowers supported on graphene nanosheets as efficient electrocatalyst for oxygen evolution reaction. Int. J. Hydrog. Energy **44**, 16120–16131 (2019)

20. D. Pletcher, X. Li, S.W.T. Price et al., Comparison of the spinels Co_3O_4 and $NiCo_2O_4$ as bifunctional oxygen catalysts in alkaline media. Electrochimica Acta **188**, 286–293 (2016)

21. X. Wang, T.T. Li, Y.Q. Zheng, Co_3O_4 nanosheet arrays treated by defect engineering for enhanced electrocatalytic water oxidation. Int. J. Hydrog. Energy **43**, 2009–2017 (2018)

22. G. Zhang, J. Yang, H. Wang et al., $Co_3O_{4-\delta}$ quantum dots as a highly efficient oxygen evolution reaction catalyst for water splitting. ACS Appl. Mater. Interfaces **9**, 16159–16167 (2017)

23. T. Zhang, Z. Li, L. Wang et al., Spinel $CoFe_2O_4$ supported by three dimensional graphene as high-performance bi-functional electrocatalysts for oxygen reduction and evolution reaction. Int. J. Hydrog. Energy **44**, 1610–1619 (2019)

24. L. Zhuang, L. Ge, Y. Yang et al., Ultrathin iron-cobalt oxide nanosheets with abundant oxygen vacancies for the oxygen evolution reaction. Adv Mater. (2017). https://doi.org/10.1002/adma.201606793

25. Y. Su, H. Liu, C. Li et al., Hydrothermal-assisted defect engineering in spinel Co_3O_4 nanostructures as bifunctional catalysts for oxygen electrode. J. Alloys Compd. **799**, 160–168 (2019)

26. F. Wang, H. Zhao, Y. Ma et al., Core-shell-structured $Co@Co_4N$ nanoparticles encapsulated into MnO-modified porous N-doping carbon nanocubes as bifunctional catalysts for rechargeable Zn–air batteries. J. Energy Chem. **50**, 52 (2020)

27. K. Elumeeva, M.A. Kazakova, D.M. Morales et al., Bifunctional oxygen reduction/oxygen evolution activity of mixed Fe/Co oxide nanoparticles with Variable Fe/Co ratios supported on multiwalled carbon nanotubes. ChemSusChem **11**, 1204–1214 (2018)

28. X. Wang, T. Ouyang, L. Wang et al., Surface reorganization on electrochemically-induced Zn-Ni-Co spinel oxides for enhanced oxygen electrocatalysis. Angew Chem. Int. Ed. Engl. **59**, 6492–6499 (2020)

29. C. Busacca, S.C. Zignani, A. Di Blasi et al., Electrospun $NiMn_2O_4$ and $NiCo_2O_4$ spinel oxides supported on carbon nanofibers as electrocatalysts for the oxygen evolution reaction in an anion exchange membrane-based electrolysis cell. Int. J. Hydrog. Energy **44**, 20987–20996 (2019)

30. G. Li, S. Hou, L. Gui et al., Carbon quantum dots decorated $Ba_{0.5}Sr_{0.5}Co_{0.8}Fe_{0.2}O_{3-\delta}$ perovskite nanofibers for boosting oxygen evolution reaction. Appl. Catal. B **257**, 117919 (2019)

31. J. Dongxiao, S. Peng, L. Fan et al., Thin MoS_2 nanosheets grafted MOFs derived porous Co-N-C flakes grown on electrospun carbon nanofibers as self-supported bifunctional catalysts for overall water splitting. J. Mater. Chem. A **5**, 23898–23908 (2017)

32. C. Alegre, C. Busacca, A. Di Blasi et al., Electrospun carbon nanofibers loaded with spinel-type cobalt oxide as bifunctional catalysts for enhanced oxygen electrocatalysis. J. Energy Storage **23**, 269–277 (2019)

33. L. Qiu, X. Han, Q. Lu et al., Co_3O_4 nanoparticles supported on N-doped electrospinning carbon nanofibers as an efficient and bifunctional oxygen electrocatalyst for rechargeable Zn-Air batteries. Inorg. Chem. Front. **6**, 3554–3561 (2019)

34. W.-H. Ryu, T.-H. Yoon, S.H. Song et al., Bifunctional composite catalysts using Co_3O_4 nanofibers immobilized on nonoxidized graphene nanoflakes for high-capacity and long-cycle $Li–O_2$ batteries. Nano Lett. **13**, 4190–4197 (2013)

35. P. Liu, J. Ran, B. Xia et al., Bifunctional oxygen electrocatalyst of mesoporous Ni/NiO nanosheets for flexible rechargeable Zn–Air batteries. Nano-Micro Lett. **12**, 1–12 (2020)

36. F. Hasché, M. Oezaslan, P. Strasser, Activity, stability and degradation of multi walled carbon nanotube (MWCNT) supported Pt fuel cell electrocatalysts. Phys. Chem. Chem. Phys. **12**, 15251 (2010)

37. S. Sukigara, M. Gandhi, J. Ayutsede et al., Regeneration of Bombyx mori silk by electrospinning—part 1: processing parameters and geometric properties. Polymer **44**, 5721–5727 (2003)

38. N.H. Chou, P.N. Ross, A. Bell et al., Comparison of cobalt-based nanoparticles as electrocatalysts for water oxidation. ChemSusChem **4**, 1566–1569 (2011)

39. A. Rebekah, E. Ashok Kumar, C. Viswanathan et al., Effect of cation substitution in $MnCo_2O_4$ spinel anchored over rGO for enhancing the electrocatalytic activity towards oxygen evolution reaction (OER). Int. J. Hydrog. Energy **45**, 6391–6403 (2020)

40. T. Maiyalagan, K.A. Jarvis, S. Therese et al., Spinel-type lithium cobalt oxide as a bifunctional electrocatalyst for the oxygen evolution and oxygen reduction reactions. Nat. Commun. **5**, 3949 (2014)

41. D.A. Robinson, K.J. Stevenson, Uniform epitaxial growth of pt on Fe_3O_4 nanoparticles; synergetic enhancement to pt activity for the oxygen reduction reaction. J. Mater. Chem. A **1**, 13443–13453 (2013)

42. J.K. Norskov, J. Rossmeisl, A.A. Logadottir et al., Origin of the overpotential for oxygen reduction at a fuel-cell cathode. J. Phys. Chem. B **108**, 17886–17892 (2004)